Supporting Information

ZrO_2 induced *d*−*d* spatial coordination effects of Ru single-atom catalysts to boost oxygen evolution reaction

Dandan Yu,[a] Bin Liu,[a] Dongming Li,[a] Junkai Yu,[a] Xijie Lan,[a] Shuhong Liu,[a] Zhuxin Li,[b] Pengyun Gao,[b] Yong Zhang*[a] and Hong Zhao*[b]

[a]School of Materials Science and Engineering, Dalian Jiaotong University, Dalian 116028, China.

[b]College of Material Science and Engineering, Sichuan University of Science & Engineering, Zigong 643000, China.

Corresponding authors

Email: zhangyong0411@126.com

Email: zhaohong@suse.edu.cn

This file contains:

Material and Reagent. chemicals and materials used in this study were obtained from commercial suppliers, and directly used without purification. Zirconyl chloride octahydrate ($ZrOCl_2 \cdot 8H_2O$, A.R.), acetate (CH_3COOH, A.R.) and ammonia solution (NH_4OH, A.R.) were purchased from Aladdin. Ruthenium chloride ($RuCl_3 \cdot 3H_2O$), isopropanol and Nafion (5 wt%) were purchased from Macklin. RuO_2 was purchased from Shandong Keyuan Biochemical Co., Ltd. Nafion 212 membrane was obtained from DuPont Co. Pt/C (60% Pt) was obtained from Johnson Matthey Company. All chemicals were utilized directly without additional purification.

Preparation of ZrO_2. 2.4 mmol $ZrOCl_2 \cdot 8H_2O$ and 3 mmol CH_3COOH were dissolved in 10 ml of deionized water as solution A. The solution A and 5% NH_4OH were slowly added dropwise into 40 ml deionized water until the pH reached 10, followed by vigorous stirring for 30 minutes. Subsequently, the product was collected by centrifugation, washed several times with deionized water, and the solution readjusted to pH 10. The mixture was transferred into a 100 ml Teflon-lined autoclave and heated at 200°C for 12 hours. After cooling to room temperature, black precipitates were obtained. The precipitates were then centrifuged, washed repeatedly with deionized water and ethanol, dried overnight in an oven at 60°C, and finally collected as ZrO_2.

Preparation of Ru-RSZ. The synthesis processes of Ru-RSZ were similar to that for ZrO_2, in which 2.4 mmol $ZrOCl_2 \cdot 8H_2O$ was replaced by 1.92 mmol $ZrOCl_2 \cdot 8H_2O$ and 0.48 mmol $RuCl_3 \cdot 3H_2O$.

Characterizations. The morphologies of the catalysts were analyzed through scanning electron microscopy (CIQTEK SEM 3000), transmission electron microscopy (TEM, FEI Titan G2),

and high-resolution TEM (HRTEM). The crystal structure was probed by X-ray powder diffraction (XRD, Empyrean PANalytical) and Raman (Horiba LabRAM HR Evolution). The surface composition of the samples was examined utilizing an X-ray photoelectron spectrometer (XPS, Thermo Scientific K-Alpha). The X-ray absorption spectroscopy (XAS) was measured at Shanghai Synchrotron Radiation Facility (BL17B1 beamline). Wavelet transformations were calculated using the WT EXAFS software.

Electrochemical Measurements. The electrochemical performances of catalysts were evaluated in a 0.5 M H_2SO_4 solution at room temperature. A standard three-electrode system was used in all measurements, with graphite rod as the counter electrode, saturated calomel electrode (saturated KCl) as the reference electrode, and platinum electrode clip with carbon paper as the working electrode. The homogeneous catalyst ink was prepared by dispersing 5 mg of samples, 500 μL of isopropanol, 500 μL of deionized water and 20 μL of Nafion solution (Dupont, 5 wt.%) under ultrasonication for 30 min. The catalyst ink was evenly coated onto the carbon paper with a loading of 0.5 mg·cm^{-2} and dried in air at room temperature. All potentials were referenced with a reversible hydrogen electrode (RHE) according to the Nernst equation ($E_{RHE} = E_{SCE} + 0.242$ V), where E_{RHE} is the potential of RHE, E_{SCE} is the potential of the saturated calomel electrode, 0.242 V is the potential difference between the saturated calomel electrode and RHE in 0.5 M H_2SO_4, which was calibrated by the CV test before electrocatalysis.

The mass activity (j_{mass}) of the Ru-RSZ and RuO_2 catalysts was determined using the following equation:

$$j_{mass} = \frac{j_{geo} \times A_{geo}}{m_{Ru}}$$

where m_{Ru} is the calculated Ru mass loaded onto carbon paper based on the results of EDS, j_{geo} is the geometric current density and A_{geo} is the geometric area.

The TOF of the Ru-RSZ and RuO_2 catalysts were calculated using the following equation, with detailed procedures described below:

$$\mathrm{TOF} = \frac{\text{Total } O_2 \text{ turnovers per } A_{geo}}{\text{Active sites per } A_{geo}}$$

The total number of O_2 turnovers per A_{geo} was calculated from the current density using the following formula:

$$\text{Total } O_2 \text{ turnover per } A_{geo} = j_{geo} \times \frac{1\ \mathrm{C \cdot s^{-1}}}{1{,}000\ \mathrm{mA}} \times \frac{1\ \mathrm{mol}}{96{,}485\ \mathrm{C}} \times \frac{1}{4} \times \frac{6.023 \times 10^{23}}{1\ \mathrm{mol\ O_2}}$$

All Ru atoms were assumed to be active sites. Therefore, the number of active sites per geometric area equals the number of Ru atoms per geometric area, which can be calculated from the total mass of Ru on the electrode and the atomic weight of Ru.[1]

The electrochemical surface area (ECSA) was estimated from the electrochemical double-layer capacitance (C_{dl}), according to the following equation:

$$\mathrm{ECSA} = \frac{C_{dl}}{C_s}$$

where C_{dl} was derived from CVs measured within the non-Faradic potential range at different scan rates. The C_s is the specific capacitance of the catalysts per unit area under identical electrolyte conditions. A value of 35.0 $\mu F \cdot cm^{-2}$ was used for C_s in this work to estimate the ECSA.[2]

The roughness factor was calculated by dividing ECSA by the geometric area of the electrode, according to the following equation:

$$R_f = \frac{ECSA}{A_{geo}}$$

where A_{geo} is the geometric area of the working electrode, which was 1 cm^2 in this study.

The specific current density per ECSA (j_{ECSA}) was estimated using the following equation:

$$j_{ECSA} = \frac{j_{geo}}{R_f}$$

where j_{geo} is the geometric current density.

Electrochemical Measurements. The membrane electrode assembly (MEA) was fabricated via the catalyst-coated membrane method using the commercial Nafion 212 membrane (N212, Dupont) with a geometric area of 1 cm^2 (1 cm × 1 cm), employing commercial Pt/C (60 wt%) as the cathode and the synthesized Ru-RSZ as the anode electrocatalyst. The Ru-RSZ electrocatalyst powder was suspended in a mixture of isopropanol, deionized water, and a Nafion (5 wt%) ethanol solution by ultrasonication for 1 h. The mass loadings of Pt/C (40%) were 0.5 $mg \cdot cm^{-2}$ for the cathode, and the mass loadings of the Ru-RSZ powder were 2 $mg \cdot cm^{-2}$ for the anode, corresponding to a Ru mass loading of 175.7 $\mu g_{Ru} \cdot cm^{-2}$. A porous Pt-plated Ti foam and carbon paper served as anodic and cathodic porous gas diffusion layers (GDLs), respectively. The membrane coated with electrocatalysts and the GDLs were hot-pressed to form the membrane electrode assembly (MEA) under 150°C and 10 MPa for 5 min. Finally, the PEM electrolysis cell was assembled by sandwiching the MEA between two titanium bipolar plates featuring serpentine flow fields. The PEMWE was maintained at 80 °C with distilled water as reactant under a flow rate of 20 $mL \cdot min^{-1}$. The polarization curves were collected from 0 to 2.0 V. The polarization curves were collected from 0 to 2.0 V. The stability of the PEMWE

was evaluated by measuring chronopotentiometry at 1 A·cm^{-2} for 100 h.

Computational Details. All the calculations were performed within the framework of the density functional theory (DFT) as implemented in the Vienna Ab initio Software Package (VASP 5.4.4) code within the Perdew–Burke–Ernzerhof (PBE) generalized gradient approximation and the projected augmented wave (PAW) method. The gamma-centered k-mash of 2×2×1 and plane-wave basis sets with cutoff energy of 450 eV were used. All structures were fully optimized until residual force was converged to 0.02 eV/Å. ZrO_2 (110) surfaces replaced by Ru atoms and RuO_2 (110) substituted were constructed to analyze the electron structure and free energy. A vacuum distance of 15 Å was used on the surface to avoid interactions. The Gibbs free energies of adsorption intermediate in AEM pathway were calculated using $\Delta G = \Delta E + \Delta ZPE - \Delta TS$, where ΔE was the binding energy, ΔZPE was zero-point energy and TS was entropy, respectively.

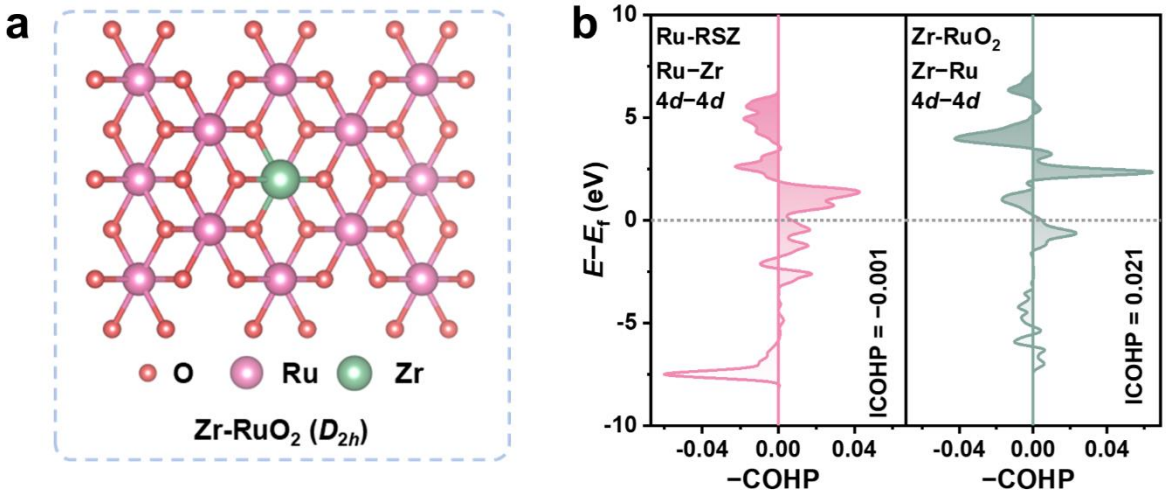

Fig. S1. (a) Model of Zr–RuO_2 with D_{2h} symmetry. (b) Calculated COHP of Ru-RSZ and Zr–RuO_2. The ICOHP for the Zr–Ru pair in Zr–RuO_2 is +0.021 eV, indicating an antibonding interaction. This contrasts with the weak bonding (−0.001 eV) observed for Ru–Zr in Ru-RSZ (D_{2d}), while resembling the antibonding nature of Ru–Ru in RuO_2 (+0.048 eV, Fig. 1b). These results indicate that the *d*–*d* orbital coupling is not solely determined by the spatial proximity of Ru and Zr, but rather depends critically on the D_{2d} coordination geometry.

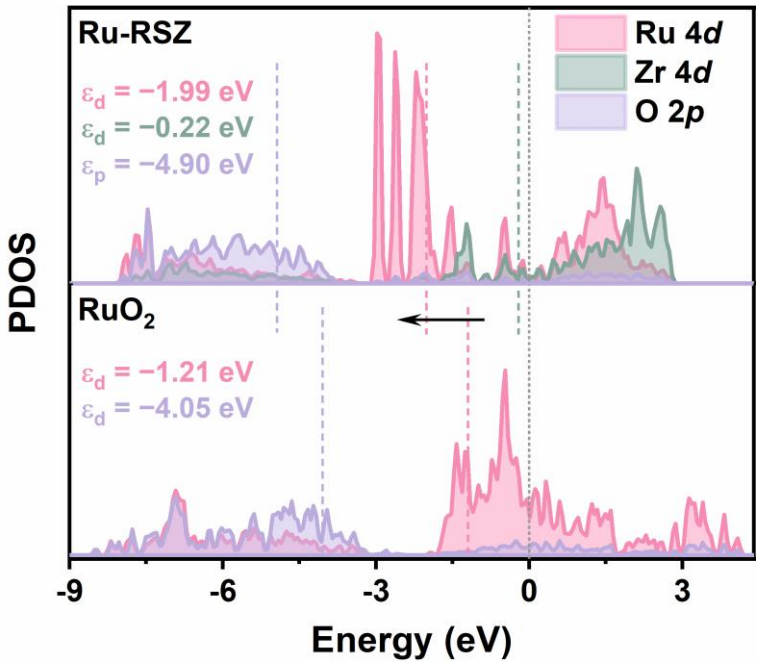

Fig. S2. The PDOS of Ru 4*d* and Zr 4*d* for Ru-RSZ and RuO_2.

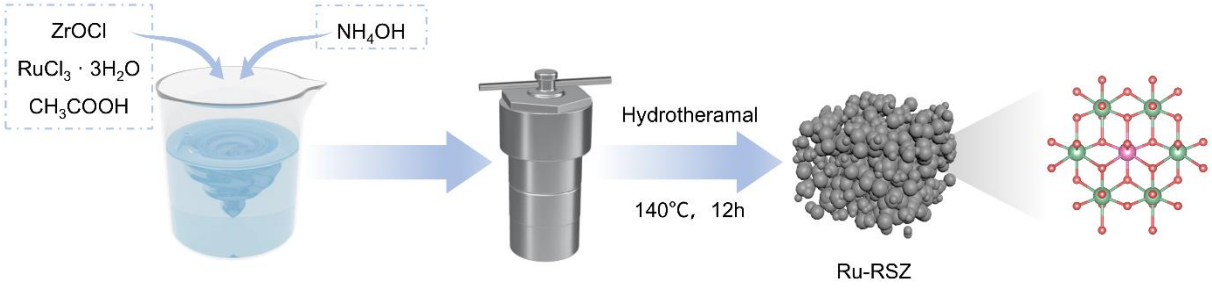

Fig. S3. Schematic representation for the synthesis of the catalysts.

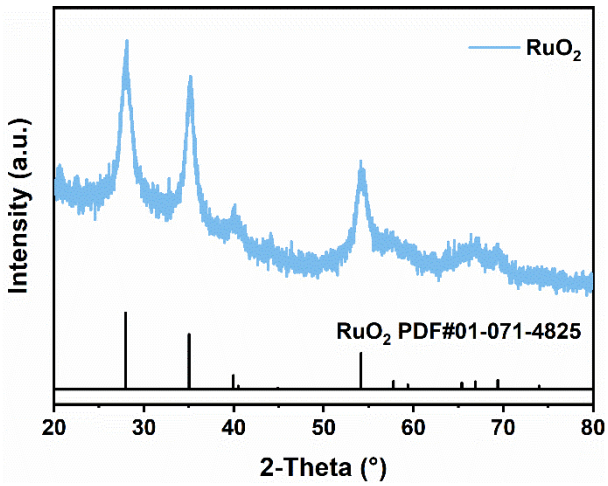

Fig. S4. XRD pattern of RuO_2.

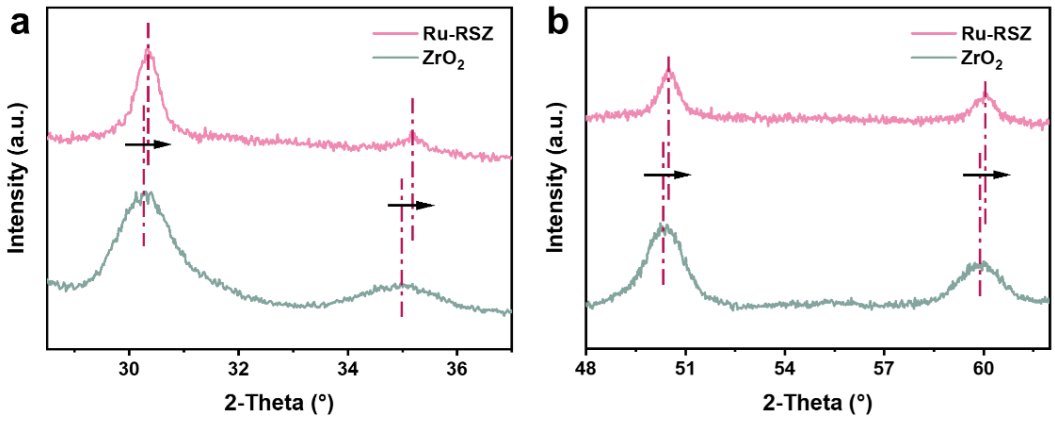

Fig. S5. (a, b) XRD patterns of different crystal planes in Ru-RSZ and ZrO_2.

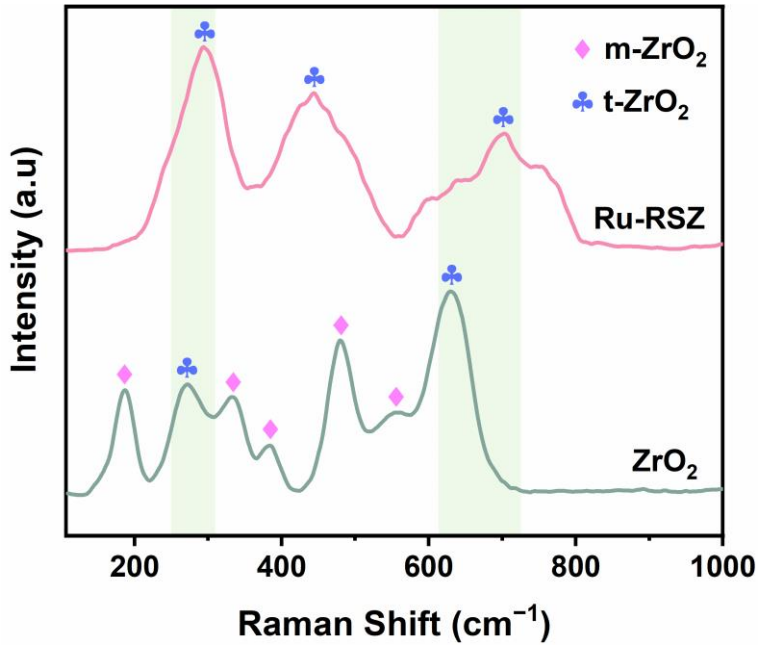

Fig. S6. Raman spectra of Ru-RSZ and ZrO_2.

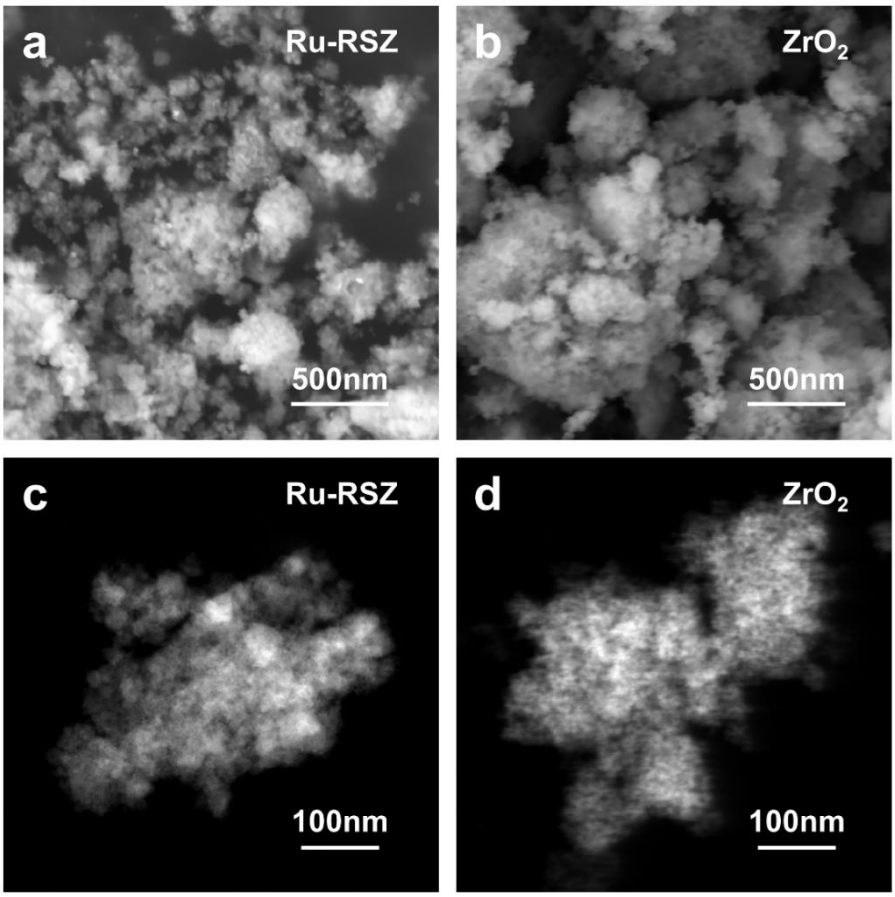

Fig. S7. (a, b) SEM images of (a) Ru-RSZ and (b) ZrO_2. (c, d) STEM images of (c) Ru-RSZ and (d) ZrO_2.

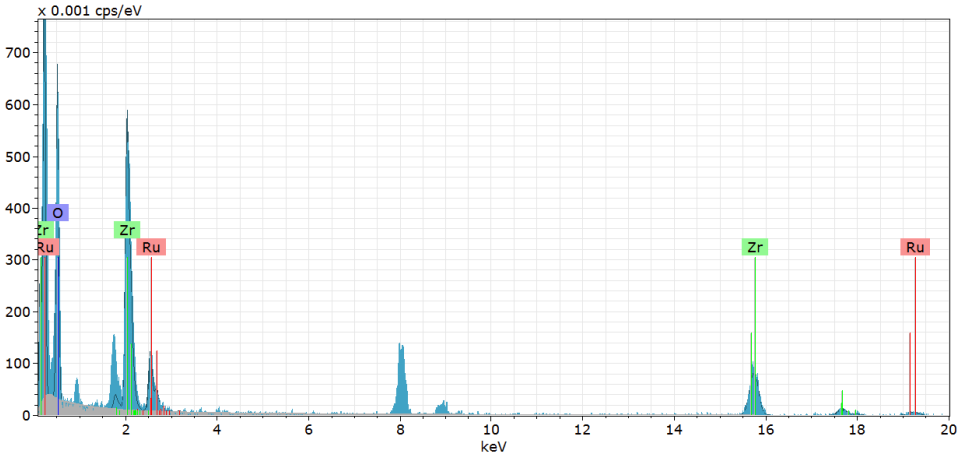

Fig. S8. Elemental spectrum of Ru-RSZ.

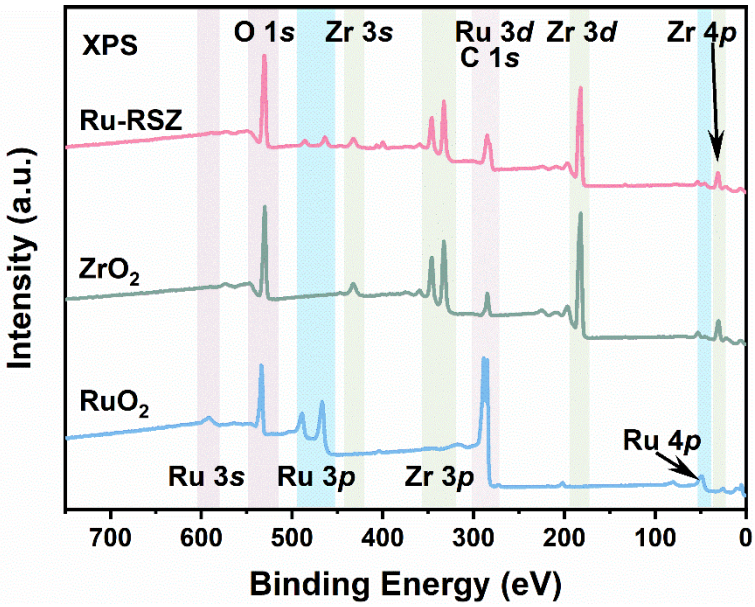

Fig. S9. XPS full spectrum of Ru-RSZ, RuO_2 and ZrO_2.

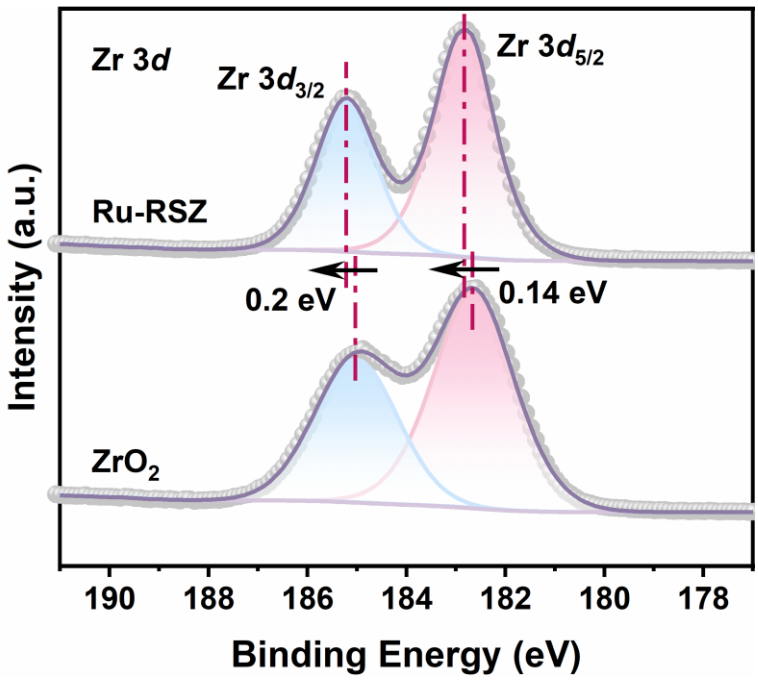

Fig. S10. XPS spectra of Ru-RSZ and ZrO_2 at the Zr 3*d* core level.

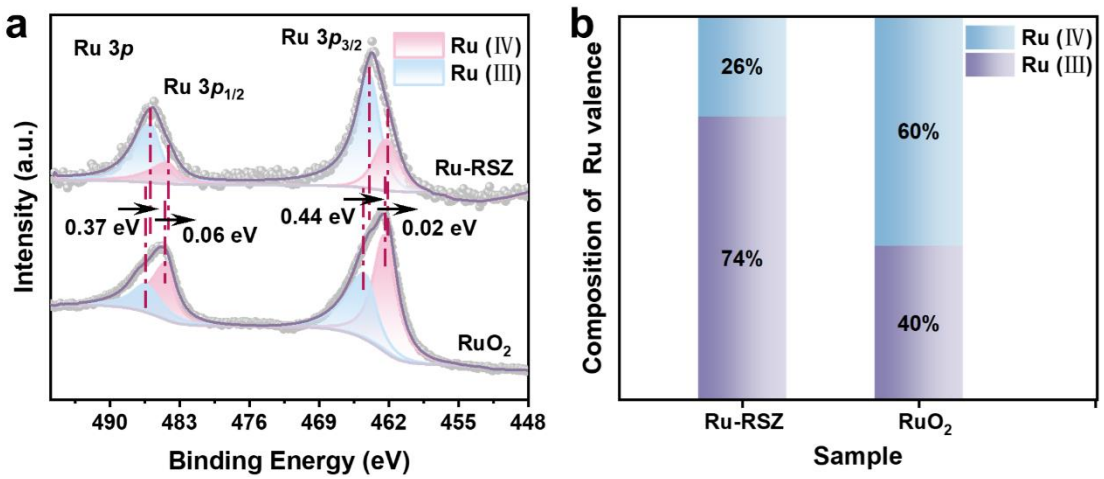

Fig. S11. (a) XPS spectra of Ru-RSZ and RuO_2 at the Ru 3*p* core level. (b) Corresponding compositions of Ru valence states in Ru-RSZ and RuO_2.

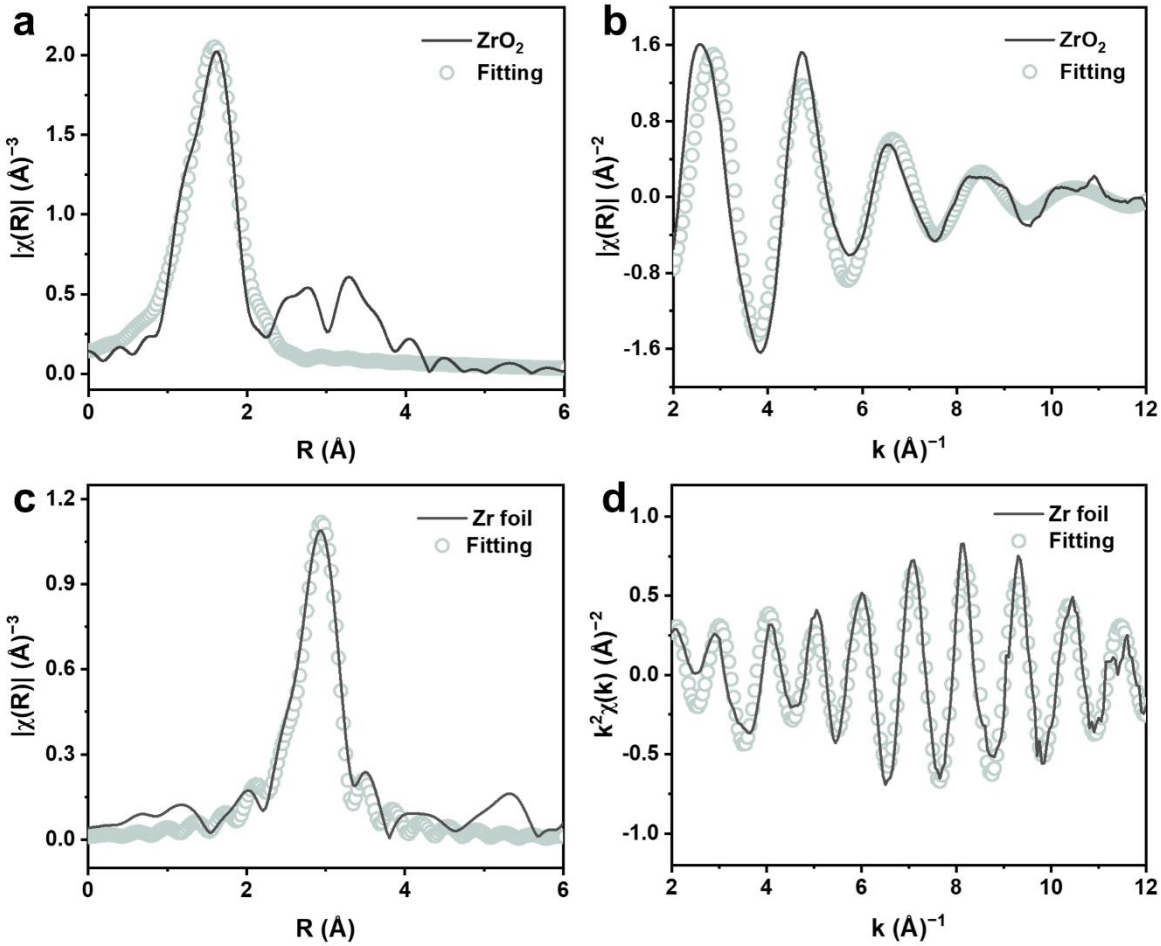

Fig. S12. R-space and k-space fitting results of Zr K-edge EXAFS spectra for (a, b) ZrO_2 and (c, d) Zr foil.

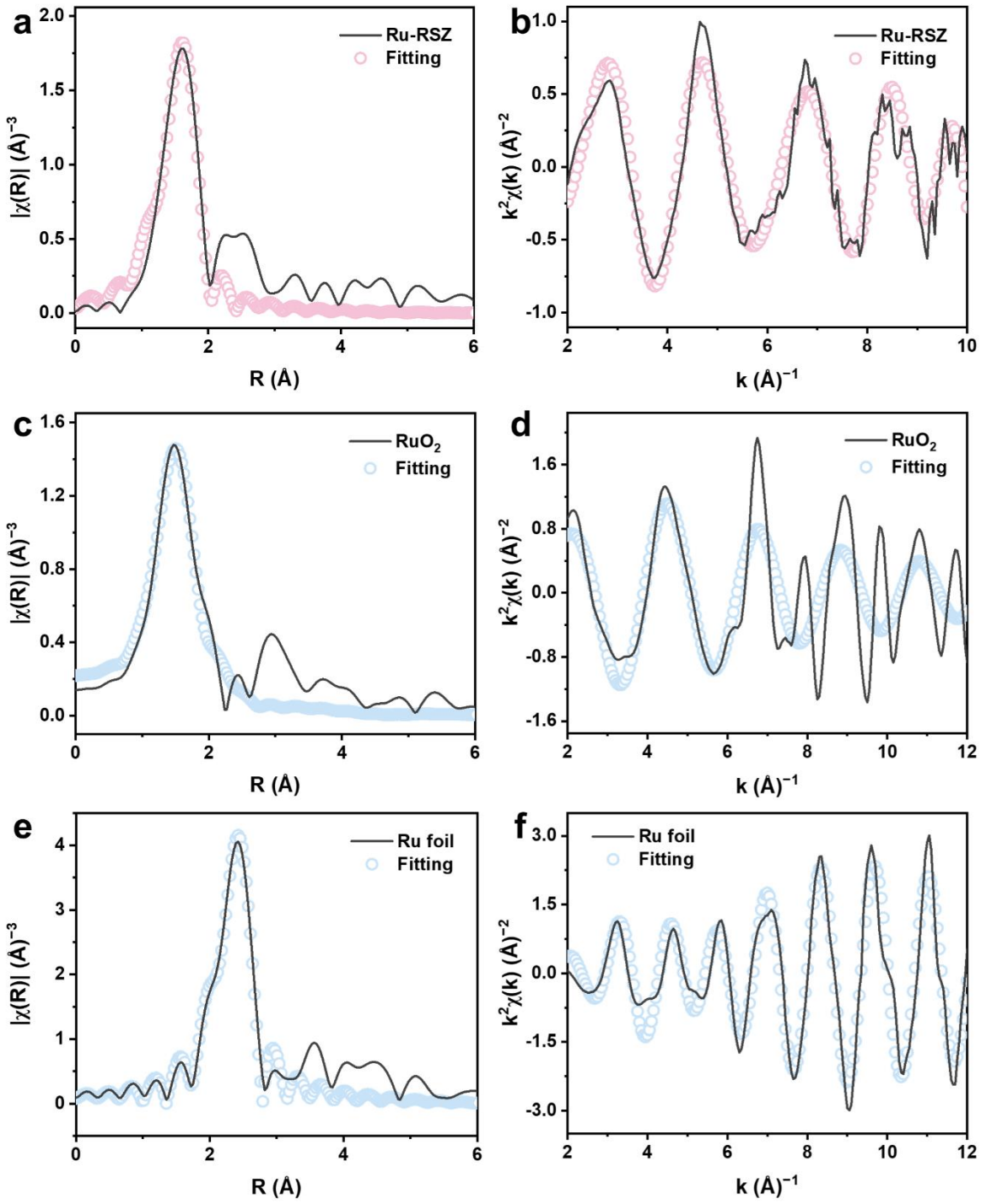

Fig. S13. R-space and k-space fitting results of Ru K-edge EXAFS spectra for (a, b) Ru-RSZ, (c, d) RuO_2 and (e, f) Ru foil.

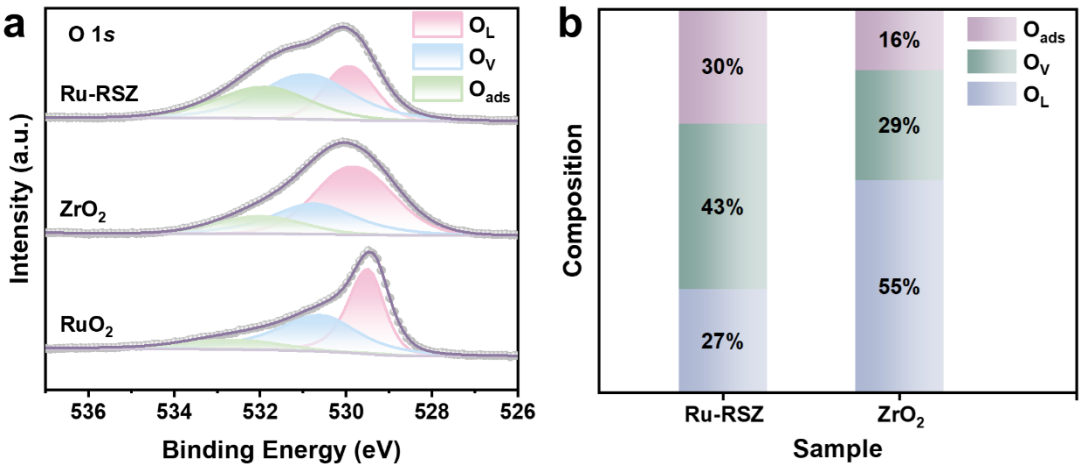

Fig. S14. (a) XPS spectra of Ru-RSZ, RuO_2 and ZrO_2 at the O 1*s* core level. (b) Corresponding composition of O valence states in Ru-RSZ and ZrO_2.

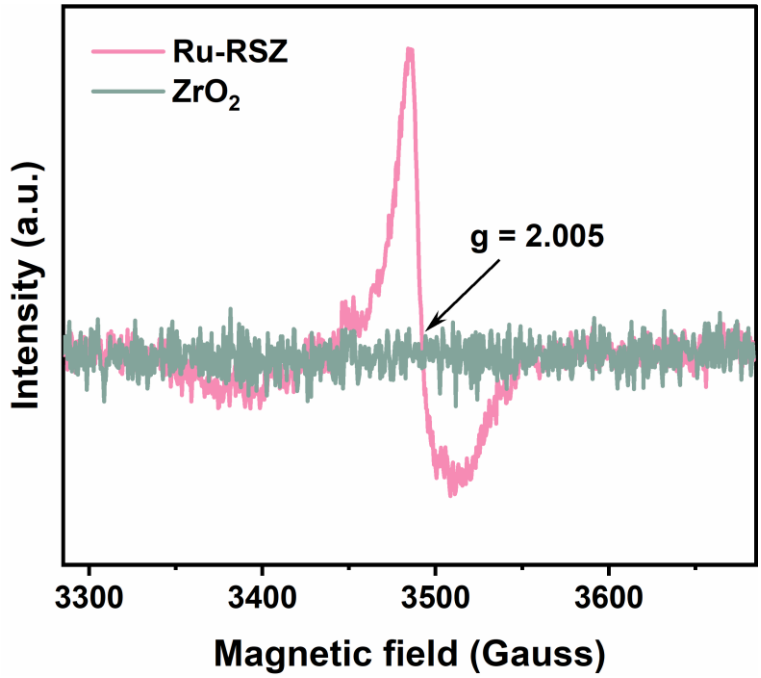

Fig. S15. EPR spectra of Ru-RSZ and ZrO.

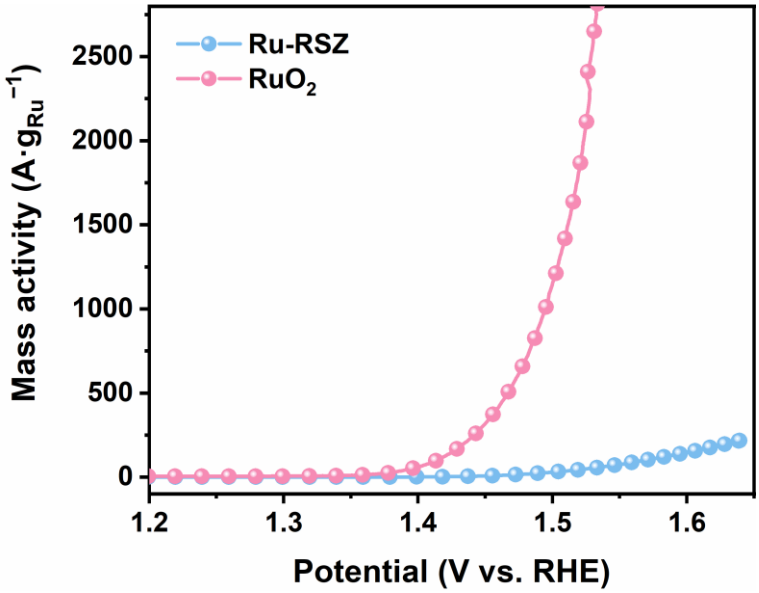

Fig. S16. Ru mass activities normalized of Ru-RSZ and RuO_2 catalysts as function of applied potential.

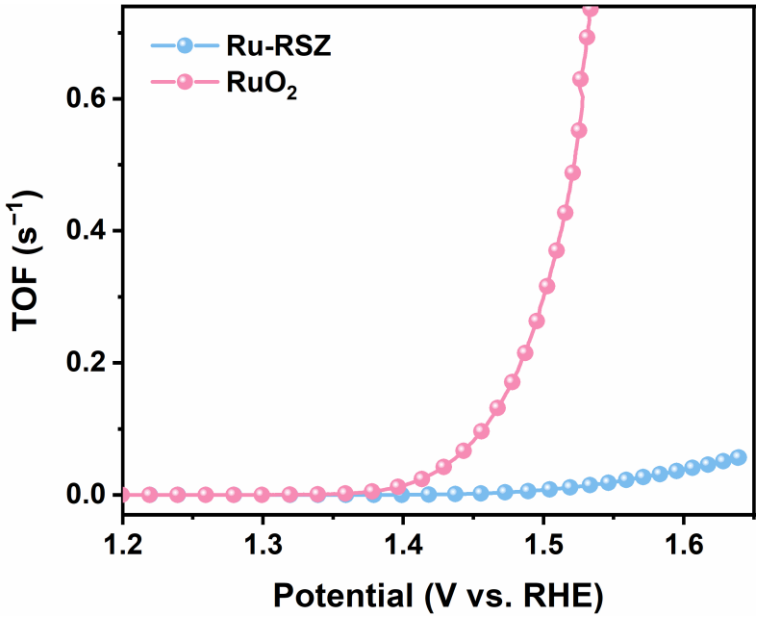

Fig. S17. The turnover frequency of the Ru-RSZ and RuO_2 catalysts calculated from polarization curves.

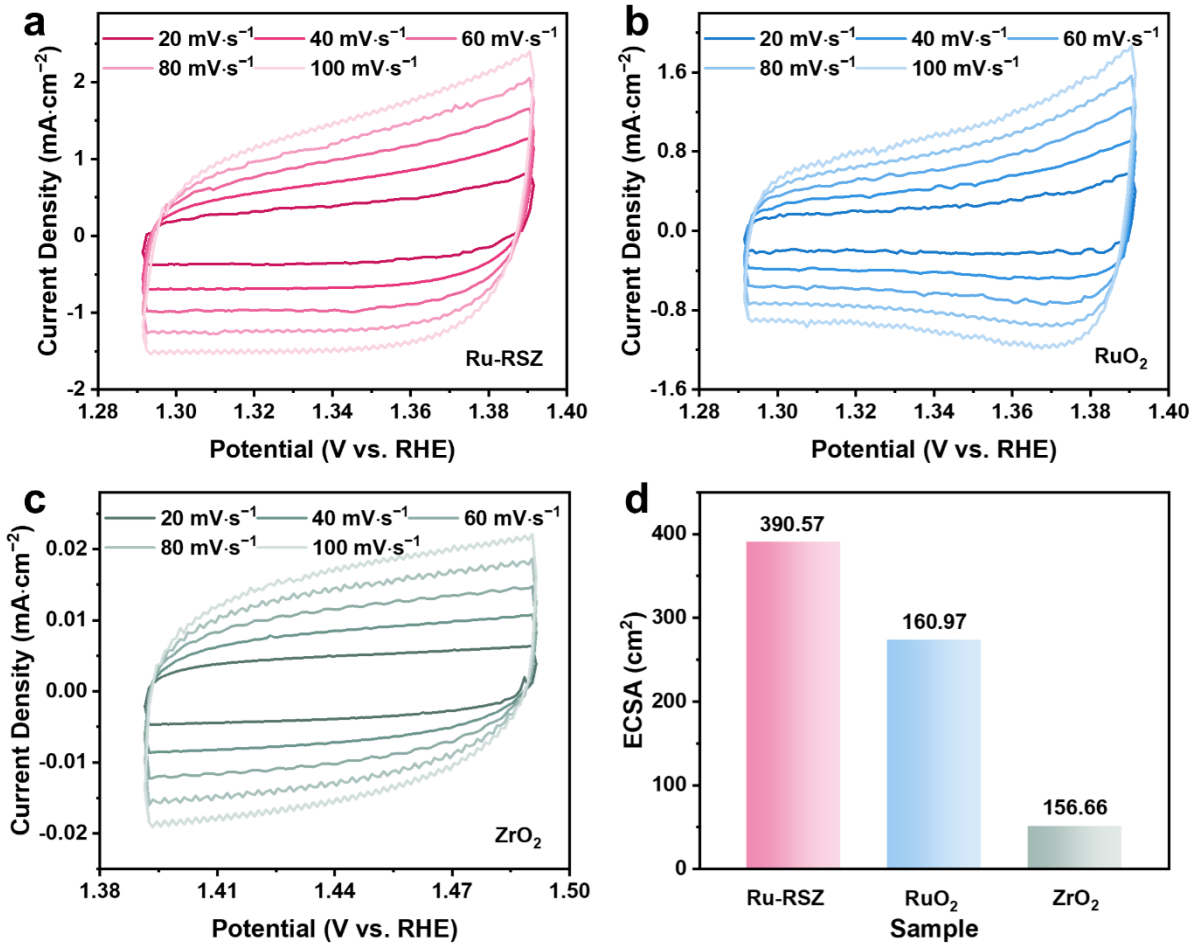

Fig. S18. CV curves of (a) Ru-RSZ, (b) RuO_2 and (c) ZrO_2 at non-Faradaic regions with various scan rates. (d) Comparison of ECSA values of Ru-RSZ, RuO_2 and ZrO_2.

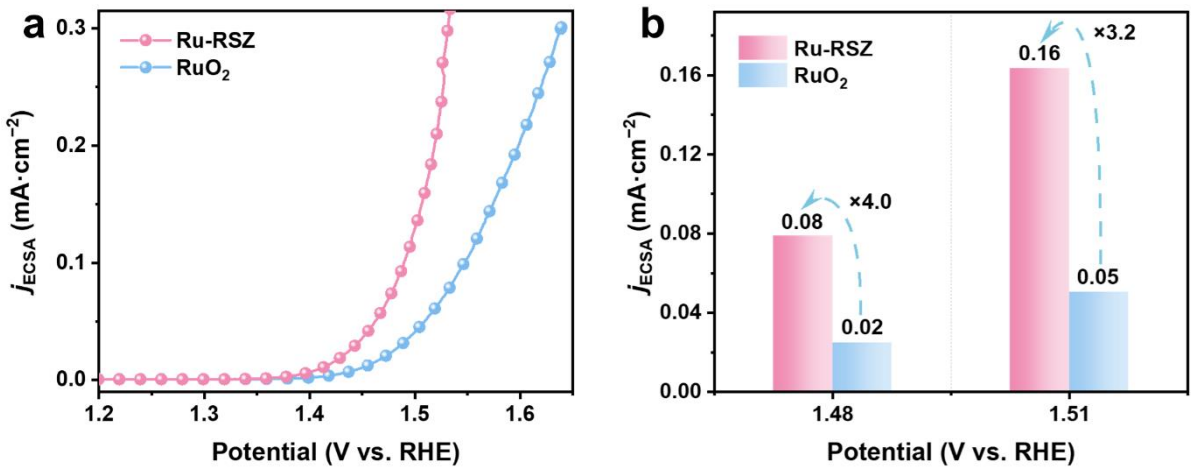

Fig. S19. (a) Ru ECSA-normalized activities of Ru-RSZ and RuO_2 catalysts. (b) ECSA normalized current densities (j_{ECSA}) of Ru-RSZ and RuO_2 at 1.48 and 1.51 V vs. RHE.

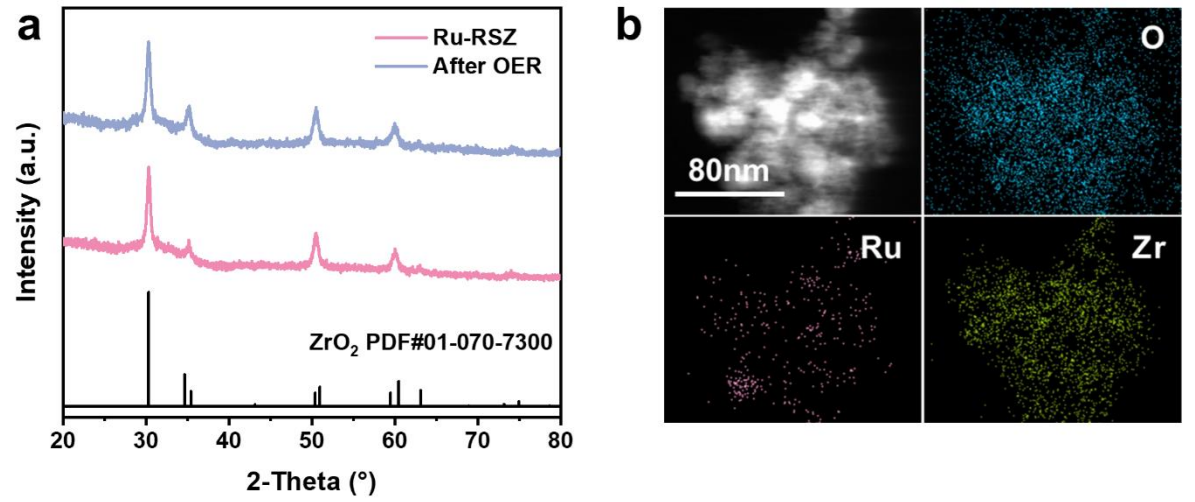

Fig. S20. Post-reaction (a) XRD pattern and (b) HAADF-STEM images of Ru-RSZ.

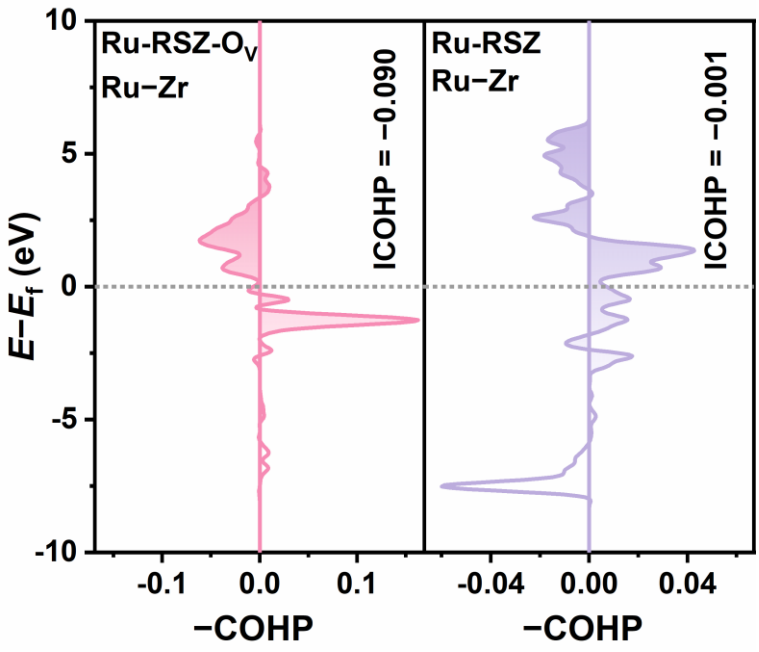

Fig. S21. Calculated COHP of Ru-RSZ-Ov and Ru-RSZ.

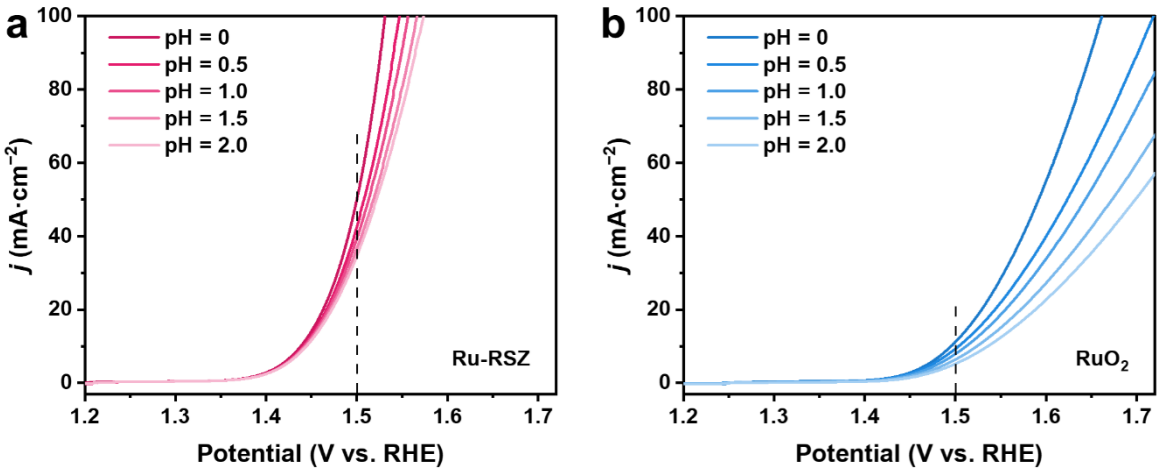

Fig. S22. LSV curves of (a) Ru-RSZ and (b) RuO_2 at different pH values.

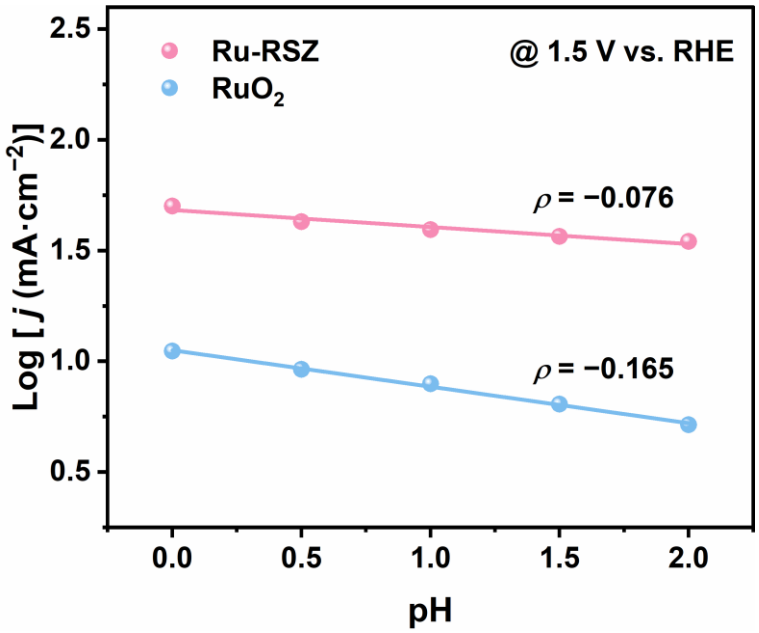

Fig. S23. pH-dependent activity of Ru-RSZ and RuO_2 at 1.5 V vs. RHE.

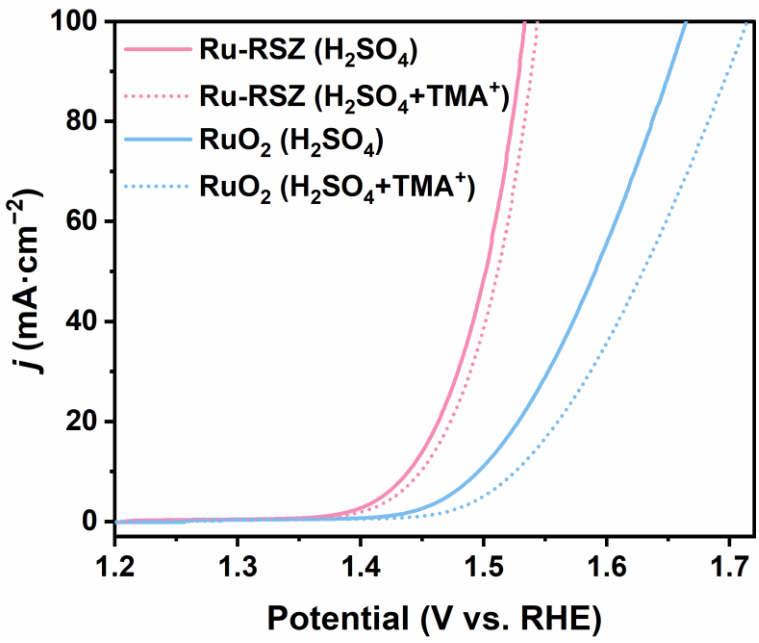

Fig. S24. LSVs with and without TMA^+ of Ru-RSZ and RuO_2 in 0.5M H_2SO_4.

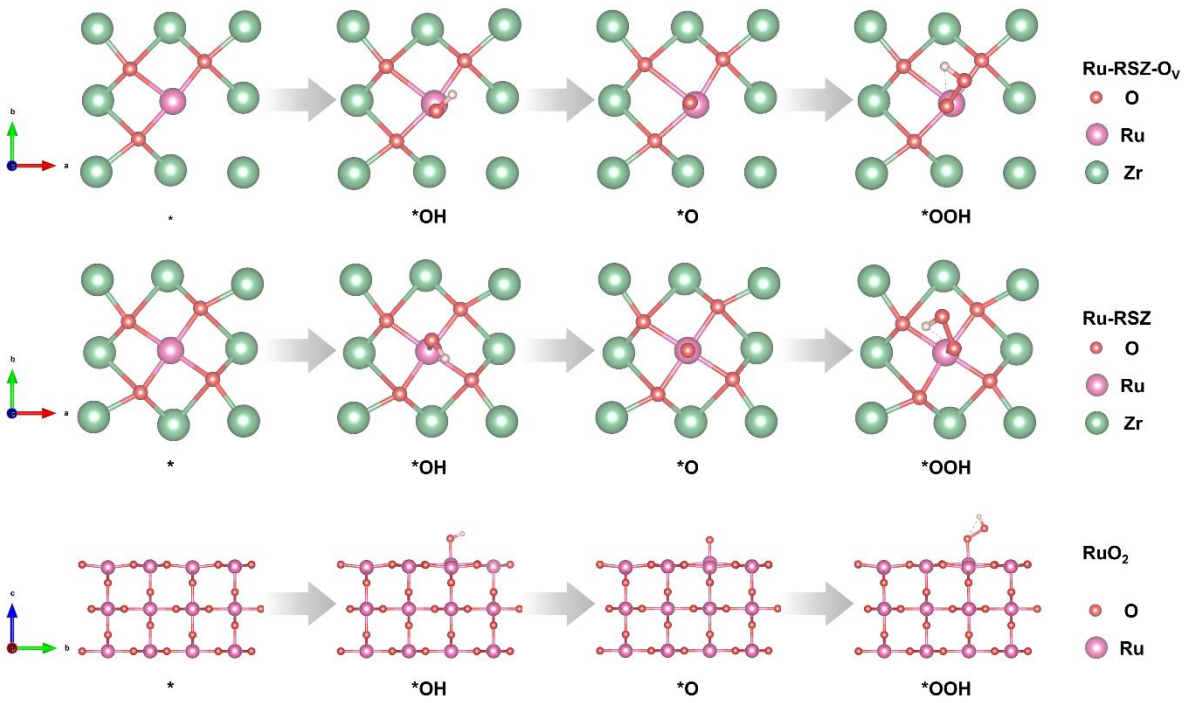

Fig. S25. Adsorption/desorption and electron transfer processes of OER intermediates on the surface of Ru-RSZ-O$_V$, Ru-RSZ and RuO_2 for AEM.

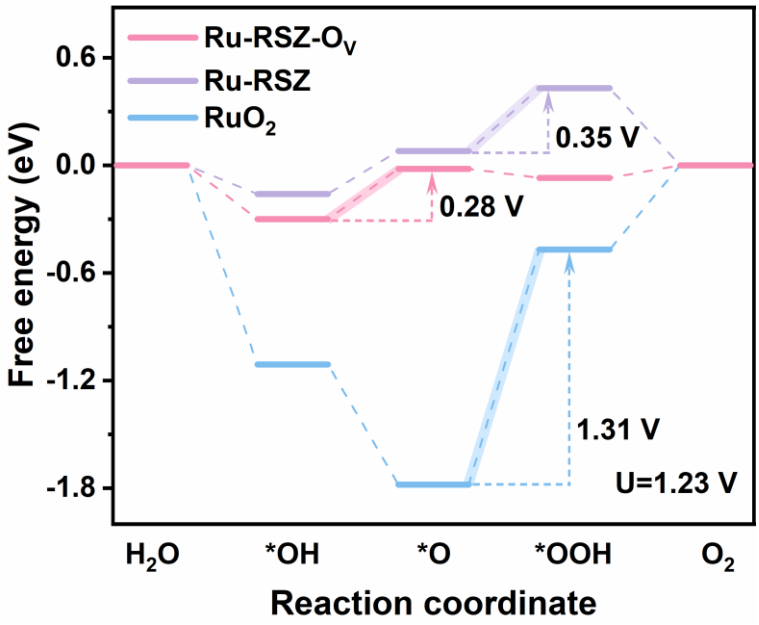

Fig. S26. Gibbs free energy diagram of Ru-RSZ-Ov, Ru-RSZ and RuO_2 at U=1.23 V.

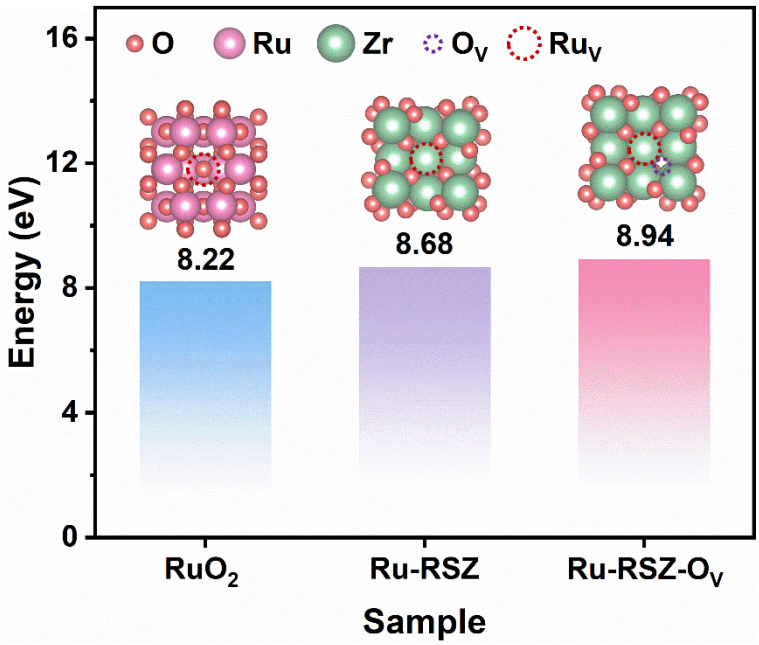

Fig. S27. Ru vacancy formation energy of Ru-RSZ-Ov, Ru-RSZ and RuO_2.

Table S1. The ratio of metallic elements in Ru-RSZ obtained by EDS

Sample	Atomic ratio (%)
Ru-RSZ	Ru: Zr = 10.8: 89.2

Table S2. XPS fitting analysis for the Ru 3*p* in Ru-RSZ and RuO_2.

Sample	Peak	Peak Position	Area	Ratio
Ru-RSZ	Ru^{4+}	462.15	17340.21	0.26
		484.14	9848.67	
	Ru^{3+}	463.85	53827.80	0.74
		485.84	22617.19	
RuO_2	Ru^{4+}	462.17	184238.48	0.60
		484.20	99813.38	
	Ru^{3+}	464.22	129873.18	0.40
		486.28	58946.26	

Table S3. The EXAFS fitting parameters at the Zr and Ru K-edge.

Sample	Path	*CN*[a]	*R*(Å)[b]	σ^2 (10^{-3})[c]	ΔE_0[d]	*R* factor
Zr foil	Zr−Zr	8*	3.21	0.008	4.7	0.0175
ZrO_2	Zr−O_1	8*	2.07	0.003	9.6	0.0123
Ru foil	Ru−Ru	12*	2.67	0.003	1.5	0.0119
RuO_2	Ru−O	6*	1.98	0.004	-4.5	0.0070
Ru-RSZ	Ru−O	7.4	2.06	0.004	8.2	0.0207

S_0^2=0.876, (fitting from Zr foil), S_0^2=0.744, (fitting from RuO_2)

[a]*CN*: coordination numbers;

[b]*R*: bond distance;

[c]σ^2: Debye-Waller factors;

[d]ΔE_0: the inner potential correction;

R factor: goodness of fit.

Table S4. XPS fitting analysis for the O 1*s* in Ru-RSZ and RuO_2.

Sample	Peak	Peak Position	Area	Ratio
Ru-RSZ	O_L	529.81	123282.02	0.30
	O_V	530.78	198955.32	0.43
	O_{ads}	531.76	137966.16	0.27
RuO_2	O_L	529.39	132727.39	0.16
	O_V	530.48	128376.55	0.29
	O_{ads}	532.45	43670.89	0.55

Table S5. Measured C_{dl} and corresponding ECSA values of different catalysts.

Sample	C_{dl} (mF·cm^{-2})	ECSA (cm^2)
Ru-RSZ	13.67	390.57
RuO_2	9.56	273.14
ZrO_2	1.77	50.57

Table S6. Fitting parameters for EIS data of different catalysts.

Sample	R_{sol} (Ω)	R_T (Ω)	C_T (F)	R_{ct} (Ω)	C_μ (mF)	χ^2, %
Ru-RSZ	1.25	0.30	0.61	1.16	0.91	1.32
RuO_2	1.23	0.84	0.53	2.35	0.93	2.26
ZrO_2	1.30	1237	0.80	2586	1.29	1.50

Table S7. OER performance metrics of Ru-RSZ and RuO_2.

Sample	η@10 mV·cm^{-2} (mV)	Tafel slope (mV·dec^{-1})	R_{ct} (Ω)	C_{dl} (mF·cm^{-2})	TOF (s^{-1})
Ru-RSZ	208	62.15	1.16	13.67	0.38
RuO_2	265	71.97	2.35	9.56	0.01

Table S8. Comparison of OER performance of Ru-RSZ with previously reported noble-metal-based electrocatalysts in acidic electrolyte.

Sample	Electrolyte	η@10 mV·cm^{-2} (mV)	Stability (h)	References
Ru-RSZ	0.5 M H_2SO_4	208	500	This work
com-RuO_2	0.5 M H_2SO_4	265	19	This work
Sb-SnO_2@RuO_x	0.5 M H_2SO_4	295	15	[3]
RuO_2-WC NPs	0.5 M H_2SO_4	347	10	[4]
PtCo-RuO_2/C	0.1 M $HClO_4$	222	20	[5]
$Ru_{0.27}Co_{2.73}O_4$	0.5 M H_2SO_4	265	100	[6]
IrRu/$T_{90}G_{10}$	0.1 M $HClO_4$	254	25	[7]
Ru_1-Pt_3Co	0.1 M $HClO_4$	280	30	[8]
Ga-RuO_2	0.5 M H_2SO_4	217.5	150	[9]
Ni-RuO_2	0.1 M $HClO_4$	214	214	[10]
ac-$Cr_{0.53}Ru_{0.47}O_{2-\delta}$	0.1 M $HClO_4$	239	40	[11]
p-L-IrO_2	0.1 M $HClO_4$	270	200	[12]
IrO_x/TiN	0.1 M $HClO_4$	293	250	[13]
Sr-$IrMnO_2$/CNTs	0.5 M H_2SO_4	236	400	[14]
$Pr_3Ir_{1-x}Mo_xO_7$	0.1 M $HClO_4$	259	200	[15]
IrO_2@TaB_2	0.1 M $HClO_4$	288	120	[16]
Ti-IrO_x/Ir	0.5 M H_2SO_4	254	100	[17]
m-RuO_2	0.5 M H_2SO_4	230	100	[18]

IrRu HNWs	0.5 M H_2SO_4	215	200	[19]
SS Pt-RuO_2 HNSs	0.5 M H_2SO_4	325	100	[20]
$ZnRuO_x$	0.5 M H_2SO_4	230	320	[21]
$RuNiO_x$	0.5 M H_2SO_4	217	100	[22]

Table S9. Bader charge of different elements.

Sample	**Bader charge of Ru element**	**Bader charge of Zr element**
Ru-RSZ-O_V	+0.3099 |e|	+1.5131 |e|
Ru-RSZ	+0.8249 |e|	+1.6345 |e|
RuO_2	+1.4893 |e|	——
ZrO_2	——	+1.2822 |e|

References

1. C. Lin, J.-L. Li, X. Li, S. Yang, W. Luo, Y. Zhang, S.-H. Kim, D.-H. Kim, S. S. Shinde, Y.-F. Li, Z.-P. Liu, Z. Jiang and J.-H. Lee, *Nat. Catal.*, 2021, **4**, 1012-1023.
2. C. Zhou, L. Li, Z. Dong, F. Lv, H. Guo, K. Wang, M. Li, Z. Qian, N. Ye, Z. Lin, M. Luo and S. Guo, *Nat. Commun.*, 2024, **15**, 9774.
3. S. Y. Park, J. W. An, J. H. Baek, H. J. Woo, W. J. Lee, S. H. Kwon and S. Bera, *ACS Appl. Mater. Interfaces*, 2023, **15**, 15332-15343.
4. S. C. Sun, H. Jiang, Z. Y. Chen, Q. Chen, M. Y. Ma, L. Zhen, B. Song and C. Y. Xu, *Angewandte Chemie International Edition*, 2022, **61**, e202202519.
5. I. Rodríguez-García, J. L. Gómez de la Fuente, J. Torrero, D. García Sánchez, M. Abdel Salam, J. A. Alonso, A. S. Gago, K. A. Friedrich, S. Rojas, M. Retuerto and Á. Tolosana-Moranchel, *J. Power Sources*, 2024, **604**, 234416.
6. G. Wang, G. Zhang and X. Chen, *Small*, 2024, **20**, e2310372.
7. I. G. Kim, A. Lim, J. H. Jang, K.-Y. Lee, I. W. Nah and S. Park, *J. Power Sources*, 2021, **501**, 230002.
8. Y. Yao, S. Hu, W. Chen, Z.-Q. Huang, W. Wei, T. Yao, R. Liu, K. Zang, X. Wang, G. Wu, W. Yuan, T. Yuan, B. Zhu, W. Liu, Z. Li, D. He, Z. Xue, Y. Wang, X. Zheng, J. Dong, C.-R. Chang, Y. Chen, X. Hong, J. Luo, S. Wei, W.-X. Li, P. Strasser, Y. Wu and Y. Li, *Nat. Catal.*, 2019, **2**, 304-313.
9. L. Wu, W. Huang, D. Li, H. Jia, B. Zhao, J. Zhu, H. Zhou and W. Luo, *Angew. Chem.*, 2024, **137**.
10. Z. Y. Wu, F. Y. Chen, B. Li, S. W. Yu, Y. Z. Finfrock, D. M. Meira, Q. Q. Yan, P. Zhu, M. X. Chen, T. W. Song, Z. Yin, H. W. Liang, S. Zhang, G. Wang and H. Wang, *Nat. Mater.*, 2023, **22**, 100-108.
11. X. Zhao, Z. Li, H. Jang, X. Wei, L. Wang, M. G. Kim, J. Cho, X. Liu and Q. Qin, *Small*, 2024, **20**, e2311172.
12. Z. Xie, X. Liang, Z. Kang, Y. Zou, X. Wang, Y. A. Wu, G. King, Q. Liu, Y. Huang, X. Zhao, H. Chen and X. Zou, *CCS Chem.*, 2025, **7**, 216-228.
13. X. Han, T. Mou, A. Islam, S. Kang, Q. Chang, Z. Xie, X. Zhao, K. Sasaki, J. A. Rodriguez, P. Liu and J. G. Chen, *J. Am. Chem. Soc.*, 2024, **146**, 16499–16510.
14. J. Kuang, B. Deng, Z. Jiang, Y. Wang and Z. J. Jiang, *Adv. Mater.*, 2023, **36**, 2306934.
15. S. Chen, S. Zhang, L. Guo, L. Pan, C. Shi, X. Zhang, Z.-F. Huang, G. Yang and J.-J. Zou, *Nat. Commun.*, 2023, **14**, 4127.
16. Y. Wang, M. Zhang, Z. Kang, L. Shi, Y. Shen, B. Tian, Y. Zou, H. Chen and X. Zou, *Nat. Commun.*, 2023, **14**, 5119.
17. Y. Wang, R. Ma, Z. Shi, H. Wu, S. Hou, Y. Wang, C. Liu, J. Ge and W. Xing, *Chem*, 2023, **9**, 2931-2942.
18. G. Zhao, W. Guo, M. Shan, Y. Fang, G. Wang, M. Gao, Y. Liu, H. Pan and W. Sun, *Adv. Mater.*, 2024, **36**, 2404213.
19. L. Tao, F. Lv, D. Wang, H. Luo, F. Lin, H. Gong, H. Mi, S. Wang, Q. Zhang, L. Gu, M. Luo and

S. Guo, *Joule*, 2024, **8**, 450-460.
20. J. Wang, H. Yang, F. Li, L. Li, J. Wu, S. Liu, T. Cheng, Y. Xu, Q. Shao and X. Huang, *Sci. Adv.*, 2022, **8**, eabl9271.
21. P. Sun, Z. Qiao, X. Dong, R. Jiang, Z. T. Hu, J. Yun and D. Cao, *J. Am. Chem. Soc.*, 2024, **146**, 15515-15524.
22. Y.-J. Ko, M. H. Han, C. Lim, S.-H. Yu, C. H. Choi, B. K. Min, J.-Y. Choi, W. H. Lee and H.-S. Oh, *J. Energy Chem.*, 2023, **77**, 54-61.